

Semihollow Core–Shell Nanoparticles with Porous SiO₂ Shells Encapsulating Elemental Sulfur for Lithium–Sulfur Batteries

Tingting Liu, Ye Zhang, Chien-Hung Li, Maria D. Marquez, Hung-Vu Tran, Francisco C. Robles Hernández, Yan Yao,* and T. Randall Lee*



Cite This: *ACS Appl. Mater. Interfaces* 2020, 12, 47368–47376



Read Online

ACCESS |



Metrics & More



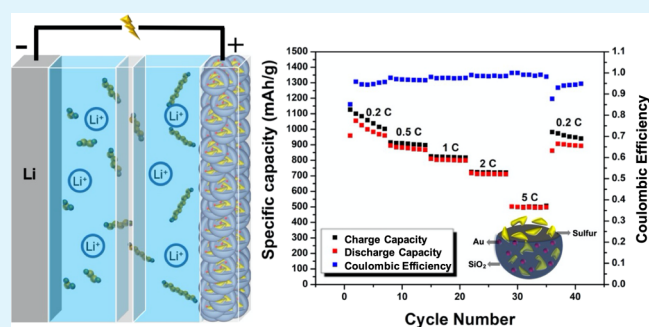
Article Recommendations



Supporting Information

ABSTRACT: Lithium–sulfur batteries have shown great promise as next-generation high energy density power sources, but their commercial applications are hindered by short battery cycle life arising from the dissolution and shuttling of polysulfides. To address this shortcoming, we prepared two types of semihollow core–shell nanoparticles in which (1) elemental sulfur is encapsulated within a porous silica shell (S@SiO₂) and (2) elemental sulfur is encapsulated within a porous silica shell where the inner surface of the shell is decorated with small Au nanoparticles (S@Au@SiO₂). These core–shell nanoparticles, both ~300 nm in diameter, were generated from analogous zinc sulfide-based core–shell nanoparticles (ZnS@SiO₂ and ZnS@Au@SiO₂, respectively) by converting the ZnS cores to elemental sulfur upon treatment with Fe(NO₃)₃. With a high surface area and strong host–polysulfide interaction, the SiO₂ shells effectively trap the polysulfides; moreover, the internal void space of these nanostructures accommodates the volume expansion of the sulfur core upon lithiation. By decorating ~5–7 nm Au nanoparticles evenly on the inner surface of the porous SiO₂ shells (i.e., S@Au@SiO₂), electron transport is enhanced, with consequently enhanced sulfur conversion kinetics at high current rates. Studies of battery performance showed that the S@SiO₂ cathode can deliver an initial capacity of 1153 mA h g⁻¹ under 0.2 C and retain 816 mA h g⁻¹ after 100 cycles. More importantly, the Au-decorated S@Au@SiO₂ cathode can deliver a high capacity of 500 mA h g⁻¹ under 5 C.

KEYWORDS: sulfur, porous SiO₂ shells, ZnS nanoparticles, Au nanoparticles, Li–S batteries



INTRODUCTION

Conventional lithium-ion batteries have gained great success as power sources for portable electric devices owing to their high energy density and long cycle life.^{1,2} However, to meet the ever-increasing demand on electric vehicles and grid-storage applications, developing alternative battery systems with increased energy density and reduced cost remains an ongoing challenge. Among the emerging energy-storage systems, lithium–sulfur (Li–S) batteries have shown great promise because of the high theoretical capacity of the sulfur cathode (1675 mA h g⁻¹) and the high abundance and low cost of elemental sulfur.^{1,3–7} Despite these advantages, the commercialization of Li–S batteries is still challenged by short battery cycle life and low Coulombic efficiency, which arise from the poor electrical conductivity of sulfur, the shuttling of intermediate lithium polysulfides, and the large volume expansion of sulfur in the cell upon lithiation (~80%).^{3,8}

To address these limitations, nanostructured materials have been designed as sulfur hosts for Li–S batteries.^{9–14} While most-studied porous carbon-based hosts improve sulfur conversion by facilitating electron transport, nonpolar carbon is a nonideal host for absorbing polar polysulfides due to weak

interactions.^{5,15,16} To strengthen the host–polysulfide interactions, inorganic oxide materials such as TiO₂,^{17,18} Al₂O₃,^{19,20} and SiO₂^{21,22} have also been used as traps for polysulfides via chemisorption and/or physisorption. Among them, SiO₂-based sulfur hosts are of special interest due to their low cost, chemical stability, and ease of synthesis using wet chemistry.²³ By constructing core–shell nanoparticles with porous SiO₂ shells and sulfur cores (i.e., S@SiO₂),^{6,24–26} the shuttling of polysulfides can be suppressed inside the shell, and the volume expansion during lithiation can be accommodated. However, due to the nonconductive nature of SiO₂, the rate performance of these cathodes is typically unsatisfactory.^{21,22,39}

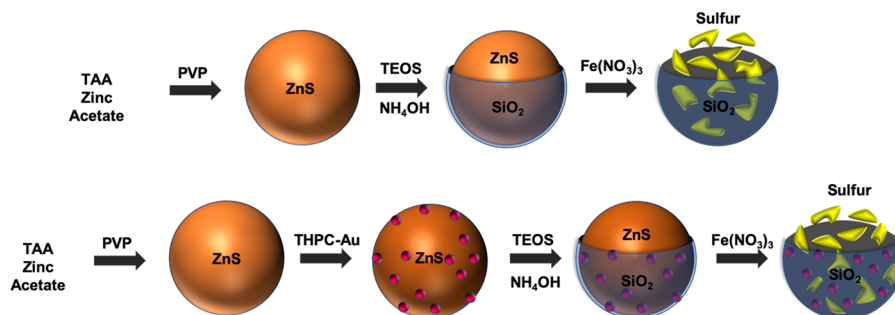
Herein, we describe a strategy for preparing silica-coated sulfur core–shell nanoparticles that involve the conversion of initial silica-coated zinc sulfide nanoparticles to sulfur cores

Received: June 6, 2020

Accepted: September 15, 2020

Published: September 15, 2020



Scheme 1. Synthesis of S@SiO₂ (Top) and S@Au@SiO₂ (Bottom) Core–Shell Nanoparticles

with a concomitant decrease in volume (see Scheme 1). This latter feature is critical to improve cycle performance due to the large volume expansion of the sulfur core upon lithiation.¹ These core–shell sulfur nanoparticles demonstrate unique properties including large surface area, low density, and high sulfur loading, which are essential for battery cathode materials. We further envisioned that the porous SiO₂ shell would inhibit the loss of sulfur by interacting strongly with the intermediate polysulfides, effectively trapping the polysulfides, and serving as a polysulfide reservoir.^{27,28} To facilitate the electron transport of the cathode, Au nanoparticles (Au NPs) were decorated on the ZnS core (ZnS@Au@SiO₂), which were subsequently converted to S@Au@SiO₂ nanoparticles upon treatment with Fe(NO₃)₃ (see Scheme 1, bottom). Moreover, strong interactions between the Au NPs and the sulfur-based discharge products (Li₂S_x, 2 ≤ x ≤ 8) further suppress the loss of sulfur.^{29,30} As a consequence, the S@SiO₂ cathodes can deliver an initial capacity of 1153 mA h g⁻¹ under 0.2 C and retain 816 mA h g⁻¹ after 100 cycles. With the Au decoration, the S@Au@SiO₂ cathodes can be cycled under 5 C with a high capacity retention of 500 mA h g⁻¹. This work shows an effective method to produce rationally designed core–shell nanostructures that provide stable Li–S battery performance.

EXPERIMENTAL SECTION

Materials. All reagents were purchased and used as received from the indicated suppliers: thioacetamide (TAA), zinc acetate dihydrate, poly(vinylpyrrolidone) (PVP, MW ~ 55k), tetraethyl orthosilicate (TEOS), 3-aminopropyltrimethoxysilane (APTMS), tetrakis(hydroxymethyl)phosphonium chloride (THPC), N-methylpyrrolidone, 1,2-dimethoxyethane (DME), and 1,3-dioxolane (DOL) were purchased from Sigma-Aldrich. Hydrogen tetrachloroaurate(III) hydrate (HAuCl₄·xH₂O) was obtained from Strem. Ammonium hydroxide (NH₄OH), hydrochloric acid (HCl), nitric acid (HNO₃), hydrogen peroxide (H₂O₂), and sulfuric acid (H₂SO₄) were purchased from Macron Fine Chemicals. Ethanol (CH₃CH₂OH) was obtained from Decon Labs Inc. Water (H₂O) was purified to a resistance of 18 MΩ·cm (Academic Milli-Q Water System; Millipore Corporation) and filtered by a 0.22 μm filter. All glassware was cleaned with aqua regia solution (3:1 concentrated hydrochloric acid: nitric acid) and piranha solution (3:1 concentrated sulfuric acid: 30% hydrogen peroxide) and dried in an oven at 60 °C before use. Lithium bis(trifluoromethylsulfonyl)imide (LiTFSI, 98+%) and lithium nitrate (LiNO₃) were purchased from Alfa Aesar and dried under vacuum at 120 °C before use. Lithium foil was also purchased from Alfa Aesar. Ketjenblack (AkzoNobel) and poly(vinylidene fluoride) (PVDF) (Sigma-Aldrich) were also used during electrode fabrication.

Synthesis of the S@SiO₂ and S@Au@SiO₂ Nanoparticles. The S@SiO₂ and S@Au@SiO₂ core–shell nanoparticles were synthesized following Scheme 1, which starts with ZnS core nanoparticles and utilizes Fe(NO₃)₃ as a key reagent in the conversion of ZnS cores to sulfur-containing cores with a concomitant decrease

in core material volume. This latter feature is critical to the success of the system due to the consequent large volume expansion of the sulfur core upon lithiation during battery operation.¹

Preparation of Zinc Sulfide Nanoparticle Cores. ZnS nanoparticles were prepared using a modification of the method reported by Xu et al.³¹ The process involves mixing zinc acetate dihydrate with thioacetamide under hydrothermal conditions. An aliquot of PVP (1.2 g; 0.022 mmol) was dissolved in 150 mL of H₂O in a 250 mL round-bottom flask; the PVP acts as a surfactant to stabilize the nanospheres. Then, zinc acetate dihydrate (0.6585 g; 3.000 mmol) was added into the PVP solution. After that, thioacetamide (0.1503 g; 2.003 mmol) was dissolved in 50 mL of H₂O and added into the PVP/zinc acetate solution at a rate of 50 mL h⁻¹. Subsequently, the solution was stirred at rt for 1 h before being heated to 100 °C and refluxed with stirring overnight. The white-colored solution indicated the successful formation of the particles. After cooling to rt, the solution was transferred into a 50 mL centrifuge tube and centrifuged at 6000 rpm for 15 min. The ZnS NPs were washed twice with 50 mL of H₂O and once with 50 mL of ethanol. The collected ZnS NPs were then redispersed in 20 mL of ethanol.

Amine-Functionalized Zinc Sulfide Nanoparticles. The amine functionalization was accomplished following a procedure by Kim et al.³² An aliquot (800 μL) of aminopropyltrimethoxysilane (APTMS) and 4 mL of the ZnS nanoparticle solution were added to 80 mL of ethanol. The mixture was heated to 80 °C and refluxed overnight to ensure complete amine functionalization of the ZnS cores. After cooling to rt, the particles were transferred into a 50 mL centrifuge tube and centrifuged at 6000 rpm for 10 min. The amine-functionalized ZnS NPs were then washed with ethanol two times, and the resulting particles were dispersed in 4 mL of ethanol.

THPC–Au Nanoparticle Preparation and Assembly on Amine-Functionalized Zinc Sulfide Core Nanoparticles. The THPC–Au nanoparticles were prepared following a report by Kim et al.³² In this procedure, 1 mL of 1 M sodium hydroxide and 2 mL of a THPC solution (25 μL of THPC in 2 mL of H₂O) were added to 90 mL of Milli-Q water in a 250 mL Erlenmeyer flask under vigorous stirring for 5 min. Then, 4 mL of 1% chloroauric acid (HAuCl₄) was added to the solution, which turned dark brown, and was stirred for 30–60 min. Afterward, the Erlenmeyer flask was stored in a refrigerator for 2 days. The solution was then concentrated to 20 mL by rotary evaporation and again stored in the refrigerator overnight.

Attachment of the THPC–Au nanoparticles to the ZnS cores was accomplished by analogy to a previously reported method.³² Briefly, 4 mL of the amine-functionalized ZnS particles were added to a 20 mL aliquot of THPC–Au solution. The solution was then placed on a shaker for 2 h and was subsequently placed in the refrigerator for 24 h. The particles were then transferred into a 50 mL centrifuge tube and centrifuged at 3000 rpm for 10 min. The NPs were washed with ethanol several times until the upper solution was transparent and clear. At this point, the particles were dispersed in 4 mL of ethanol.

SiO₂-Coated Zinc Sulfide Core–Shell Nanoparticles (ZnS@SiO₂). To obtain both types of SiO₂-coated ZnS core–shell nanoparticles, we employed a modification of the method reported

by Stöber et al.³³ As a representative example, 4 mL of the ZnS particles in 20 mL of ethanol were subjected to sonication for 1 h. Then, 0.4 mL of $\text{NH}_3\cdot\text{H}_2\text{O}$, 1 mL of H_2O , and 40 μL of tetraethyl orthosilicate (TEOS) were added to the solution and stirred for 2 h to obtain the silica-coated particles (~ 15 nm) at rt. The particles were next transferred into a 50 mL centrifuge tube and centrifuged at 6000 rpm for 10 min. The resulting $\text{ZnS}@/\text{SiO}_2$ nanoparticles were washed with ethanol and then redispersed in 4 mL of ethanol. The gold silica-coated zinc sulfide nanoparticles ($\text{ZnS}@/\text{Au}@/\text{SiO}_2$) were synthesized following an analogous procedure.

SiO_2 -Coated Sulfur Core–Shell Nanoparticles ($\text{S}@/\text{SiO}_2$). Silica-coated sulfur nanoparticles were prepared following the methodology reported by Du et al.³⁴ As a representative example, $\text{ZnS}@/\text{SiO}_2$ core–shell nanoparticles were dried at 60 °C in an oven for 3 h. The dried $\text{ZnS}@/\text{SiO}_2$ nanoparticles (40 mg) were dispersed in 10 mL of 0.3 M $\text{Fe}(\text{NO}_3)_3$ and stirred for 24 h in an ice bath. The nanoparticles were then centrifuged at 6000 rpm for 10 min, washed with 20 mL of H_2O , and then dried at 60 °C for 3 h to give the $\text{S}@/\text{SiO}_2$ core–shell nanoparticles. The silica-coated sulfur-gold core–shell nanoparticles ($\text{S}@/\text{Au}@/\text{SiO}_2$) were synthesized following an analogous procedure.

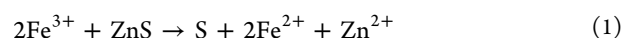
Nanoparticle Characterization. The morphologies of all nanoparticles were characterized using a scanning electron microscope (SEM, LEO-1525) operating at an accelerating voltage of 15 kV. All SEM samples were deposited on silicon wafers. For an additional perspective, the nanoparticles were also evaluated using a JEM-2100 FX transmission electron microscope (TEM) operating at an accelerating voltage of 200 kV equipped with an energy-dispersive X-ray spectroscopy (EDX) apparatus. All TEM samples were deposited on 300 mesh holey carbon-coated copper grids. Additional EDX data were collected at 18 kV by an EDX attached to a Nova NanoSEM 230 microscope. X-ray diffraction (XRD) patterns were obtained using a PANalytical X'Pert PRO X-Ray Diffractometer. Thermogravimetric analysis (TGA) was carried out by a Hi-Res TGA thermogravimetric analyzer under nitrogen gas (N_2) with a 10 °C min^{-1} heating rate.

Electrochemical Studies. The battery cathode was prepared by the slurry-cast method. A 60 wt % cathode ($\text{S}@/\text{SiO}_2$ or $\text{S}@/\text{Au}@/\text{SiO}_2$ nanoparticles), 30 wt % Ketjenblack, and 10 wt % PVDF were mixed in *N*-methylpyrrolidone. The resulting slurry was evenly applied onto carbon paper and dried in a 60 °C vacuum oven overnight. The areal mass loading of the active material was 2 mg cm^{-2} , which is greater than that for a related Au NP-based battery system,²⁹ but still warrants improvement for practical applications. The electrolyte used was 1 M LiTFSI and 0.2 M LiNO_3 dissolved in the mixture of 1,2-dimethoxyethane (DME) and 1,3-dioxolane (DOL) (volume ratio 1:1). The electrolyte/sulfur ratio was optimized at 15 $\mu\text{L mg}^{-1}$. A lower electrolyte/sulfur ratio (5 $\mu\text{L mg}^{-1}$) led to insufficient wetting of the electrode and low capacity (Figure S1). The electrochemical performance of the cathode was evaluated in 2032 coin cells assembled inside an argon-filled glovebox (oxygen <0.1 ppm, moisture <0.5 ppm) using Celgard as the separator and lithium foil as the anode. The charge/discharge cycling test was performed with a voltage range of 1.8–3 V vs Li/Li^+ using a Land battery testing system.

RESULTS AND DISCUSSION

Synthetic Strategy. The strategy used to prepare both the $\text{S}@/\text{SiO}_2$ and $\text{S}@/\text{Au}@/\text{SiO}_2$ nanoparticles is illustrated in Scheme 1. Both types of nanoparticles begin with the formation of the ZnS nanoparticle cores. For the $\text{S}@/\text{Au}@/\text{SiO}_2$ nanoparticles, the ZnS NPs were first functionalized with an amine-terminated silane (APTMS), which renders the surface positively charged and enables subsequent electrostatic attachment of the Au NPs.³² The following step, for both types of NPs, involves growing the SiO_2 shell. The final key step in the core–shell nanoparticle preparations is the reduction of the

ZnS by Fe^{3+} to yield semihollow elemental sulfur cores, according to the equation³⁴



Due to the loss of mass associated with zinc, the structure of the nanoparticles changes from a core–shell structure (e.g., $\text{ZnS}@/\text{SiO}_2$) to a semihollow structure with elemental sulfur encapsulated within a porous SiO_2 shell (e.g., $\text{S}@/\text{SiO}_2$), providing capacity for volumetric expansion needed for the formation of intermediate lithium polysulfides. The structural change from $\text{ZnS}@/\text{SiO}_2$ and $\text{ZnS}@/\text{Au}@/\text{SiO}_2$ core–shell nanoparticles into semihollow $\text{S}@/\text{SiO}_2$ and $\text{S}@/\text{Au}@/\text{SiO}_2$ core–shell nanoparticles can be monitored via SEM, as illustrated in Figure 1.³⁵

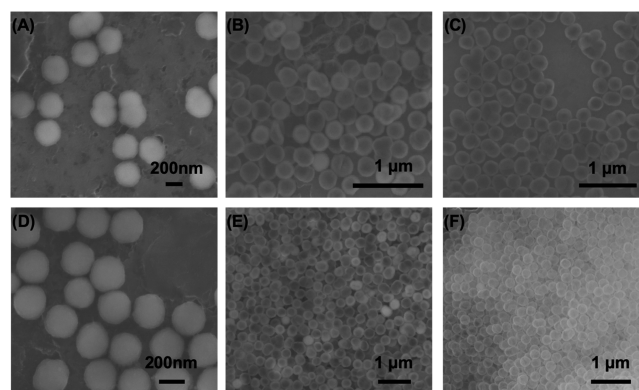


Figure 1. SEM images monitoring the $\text{Fe}(\text{NO}_3)_3$ reduction of $\text{ZnS}@/\text{SiO}_2$ (A–C) and $\text{ZnS}@/\text{Au}@/\text{SiO}_2$ (D–F) nanoparticles after (A, D): 0, (B, E): 12, and (C, E): 24 h at 0 °C, respectively.

Morphology and Composition of the Nanoparticles.

Both SEM and TEM were used to follow the development of the core–shell $\text{S}@/\text{SiO}_2$ and $\text{S}@/\text{Au}@/\text{SiO}_2$ nanoparticles and are shown in Figure 2. The ZnS nanoparticles are approximately 270 nm in diameter, as determined by the SEM image in Figure 2A. A typical TEM image of the silica-coated ZnS nanoparticles ($\text{ZnS}@/\text{SiO}_2$) is provided in Figure 2B and shows a SiO_2 shell thickness of ~ 15 nm, yielding core–shell $\text{ZnS}@/\text{SiO}_2$ nanoparticles ~ 300 nm in diameter. The final $\text{S}@/\text{SiO}_2$ nanoparticles were characterized by TEM and are

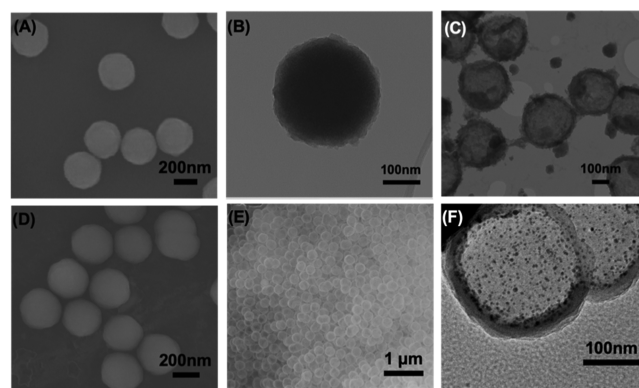


Figure 2. (A) SEM image of the ZnS nanoparticles. (B) TEM image of the core–shell $\text{ZnS}@/\text{SiO}_2$ nanoparticles. (C) TEM image of the core–shell $\text{S}@/\text{SiO}_2$ nanoparticles. (D) SEM image of the core–shell $\text{ZnS}@/\text{Au}@/\text{SiO}_2$ nanoparticles and (E, F) SEM and TEM images of the core–shell $\text{S}@/\text{Au}@/\text{SiO}_2$ nanoparticles.

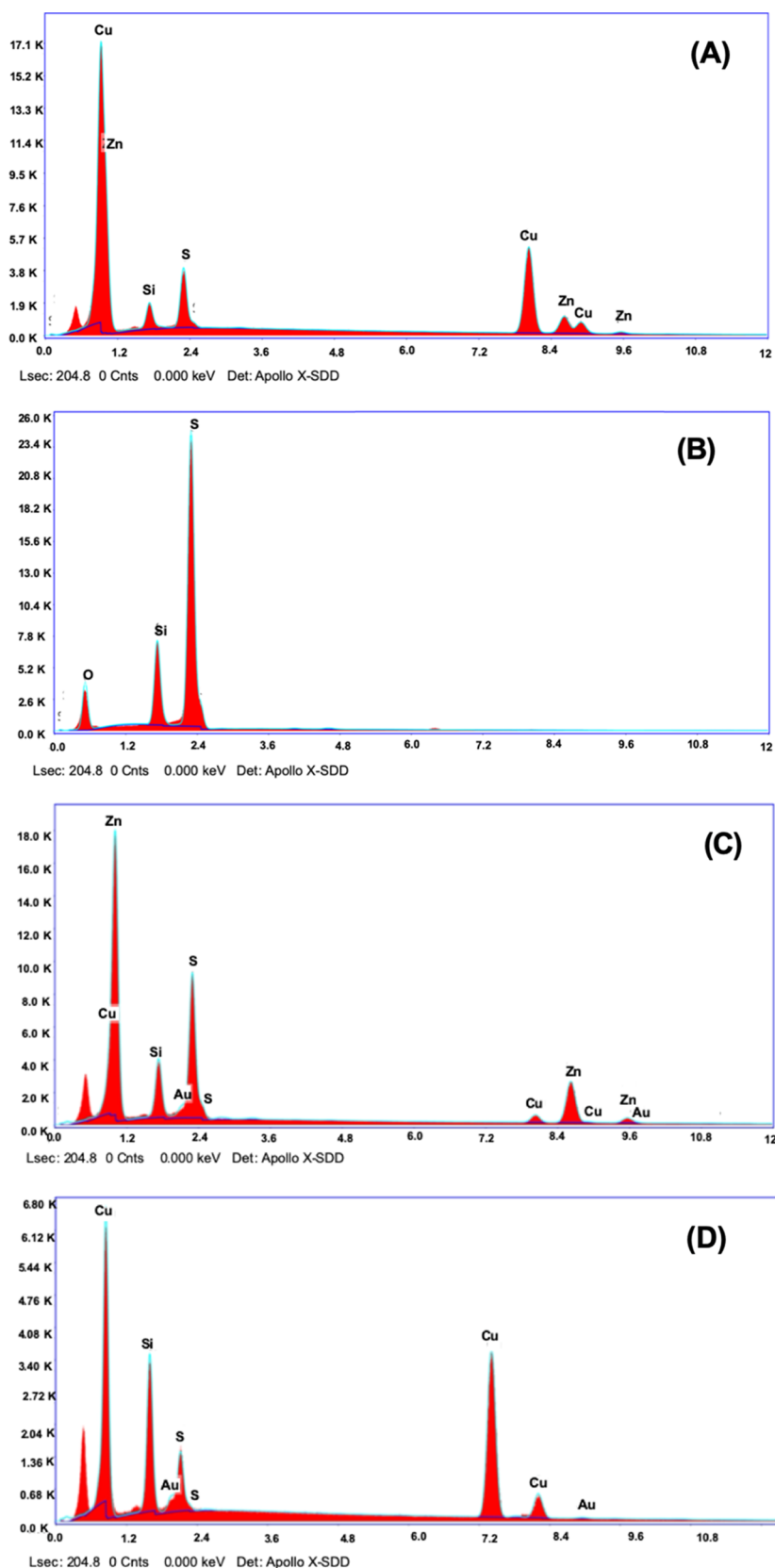


Figure 3. SEM-EDX spectra of (A) core-shell ZnS@SiO₂ nanoparticles, (B) core-shell S@SiO₂ nanoparticles, (C) core-shell ZnS@Au@SiO₂ nanoparticles, and (D) core-shell S@Au@SiO₂ nanoparticles. SEM-EDX samples were prepared on copper tape-covered Si wafers.

shown in Figure 2C. The diameter of the final composite nanoparticles remains in the 300 nm range, demonstrating that the reduction step has no negative effects on the outer silica

shell. Also apparent from the TEM images is the void space within the nanostructure, which can preserve the structural integrity of the shell during the discharge process. A typical

SEM image of the core–shell ZnS@Au@SiO₂ nanoparticles is shown in Figure 2D. The diameter of the ZnS@Au@SiO₂ nanoparticles is also ~300 nm, proving that the existence of Au seeds has no impact on the thickness of the SiO₂ coating. The final S@Au@SiO₂ nanoparticles were characterized by both SEM (Figure 2E) and TEM (Figure 2F). The TEM image (Figure 2F) also shows the presence of the Au NPs, which were not observed by SEM since the majority of the Au NPs located inside the SiO₂ shell, have a diameter of ~5–7 nm. Overall, the size and morphology of the S@SiO₂ nanoparticles were identical to those of the S@Au@SiO₂ nanoparticles, which indicates that the addition of the Au NPs has no substantial impact on the size and morphology of the final composite NPs.

Furthermore, the ZnS@SiO₂, S@SiO₂, ZnS@Au@SiO₂, and the S@Au@SiO₂ nanoparticles were characterized by SEM-EDX to determine their elemental composition. The EDX spectra of the nanoparticles are shown in Figure 3A–D. It is important to note the presence of Zn in the ZnS@SiO₂ sample at 8.64 keV in the EDX spectrum (Figure 3A) and the absence of this peak in the EDX spectrum of the S@SiO₂ nanoparticles (Figure 3B). Additionally, there is no clear evidence of Fe, at 6.40 keV, in the EDX results of the S@SiO₂ nanoparticles (Figure 3B), and the presence of the S peak at 2.31 keV implies the successful and entire conversion of the ZnS core into elemental sulfur inside the silica shell as well as complete removal of Zn²⁺, Fe²⁺, and Fe³⁺ ions during the final washing steps. Elemental analyses of the ZnS@Au@SiO₂ and S@Au@SiO₂ nanoparticles were also studied by SEM-EDX (Figure 3C,D). Both nanoparticles show the presence of Au, which partially overlaps with the S peak at 2.12 keV. Note, the appearance of Cu in the SEM-EDX spectra of both samples originated from the copper tape and sample holder used for the EDX analysis.

Imaging and elemental mapping of the S@Au@SiO₂ nanoparticles by TEM illustrate the presence of Si, O, S, and Au, but no Zn was observed (see Figure 4A), consistent with the aforementioned EDX analysis by SEM (Figure 3D). High-resolution TEM micrographs show the presence of crystalline Au particles with sizes ranging from 5 to 7 nm (Figure 4B,C). An in-depth characterization of the Au particles confirms the *d*-spacing typical of the {111} planes, leading to the conclusion

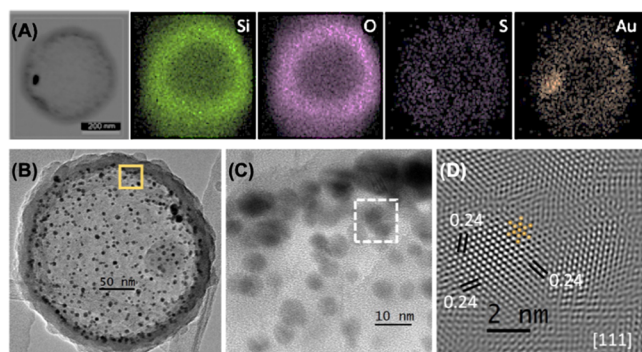


Figure 4. (A) TEM image of the S@Au@SiO₂ nanoparticles and element mapping for silicon, oxygen, sulfur, and gold. (B, C) High-resolution TEM images of the S@Au@SiO₂ nanoparticles in different scales. (D) High-resolution TEM micrographs of S@Au@SiO₂ nanoparticles with measured *d*-spacing of the {111} crystal plane of gold. The numerical simulation was carried out using the Vesta software.

that the particle orientation is along the [111] zone axis. Numerical simulations of the atomic distribution along the [111] direction show an almost perfect match between the experimental work (Figure 4D) and the simulated projection using Vesta software, further confirming that the particles are Au.

To provide additional support for the existence of sulfur inside the core–shell nanoparticles, analyses by X-ray diffraction (XRD) were performed. Figure 5A shows the

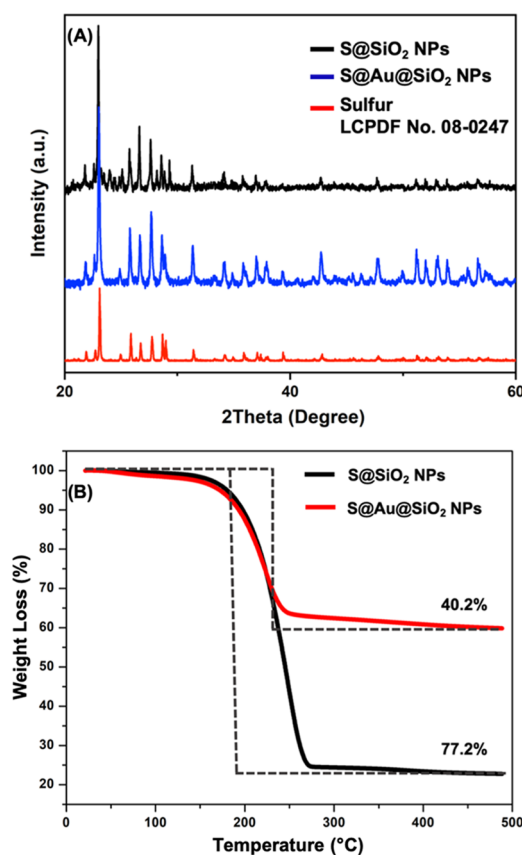


Figure 5. (A) XRD spectra of the S@SiO₂ (black), S@Au@SiO₂ (blue) nanoparticles, and standard sulfur JCPDS no. 08-0247 (red). (B) TGA curves for the S@SiO₂ (black) and S@Au@SiO₂ (red) nanoparticles.

diffraction pattern of the S@SiO₂ nanoparticles and S@Au@SiO₂ nanoparticles; notably, the typical pattern for sulfur (JCPDS no. 08-0247) was observed, further confirming the complete conversion of the ZnS core to an elemental sulfur core. Due to the small amount of gold, the XRD spectra were unable to demonstrate the presence of gold. The sulfur content of both nanoparticles was determined using thermogravimetric analysis (TGA; see Figure 5B). For our nanoparticles, the weight loss can be attributed to the evaporation of sulfur. TGA experiments were performed under nitrogen flow from 25 to 500 °C at a heating rate of 10 °C min⁻¹. The TGA curves in Figure 5B show a 77.2 and 40.2% weight loss for the S@SiO₂ and S@Au@SiO₂ nanoparticles, respectively. The lower sulfur percentage loss for the S@Au@SiO₂ nanoparticles compared to the S@SiO₂ nanoparticles can be attributed to the presence of high-density elemental gold in only the former samples; more precisely, if we remove the mass of Au from the S@Au@SiO₂ samples and recalculate, the sulfur percentage loss for the

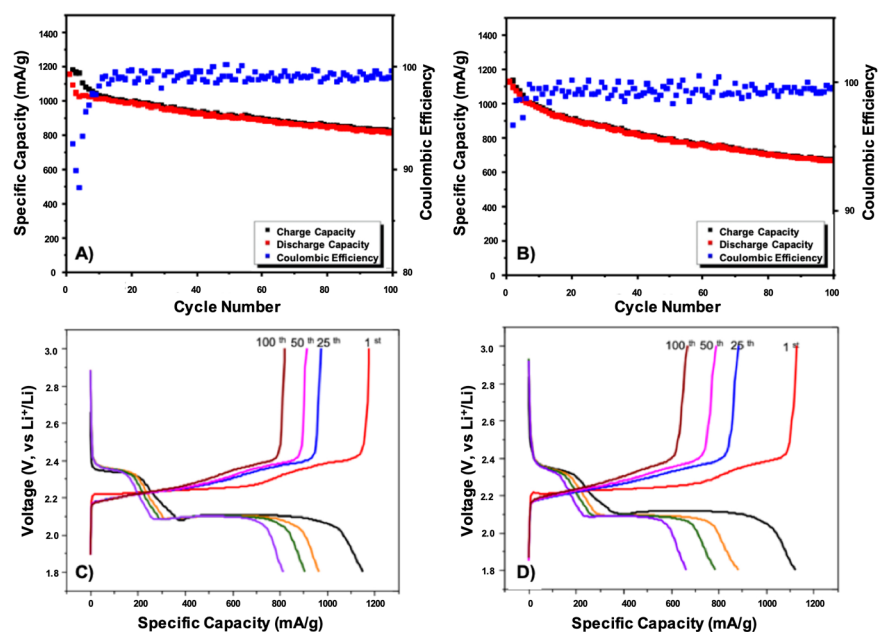


Figure 6. (A, B) Galvanostatic charge/discharge cycling performance and (C, D) voltage profiles at a current density of 0.2 C for the S@SiO₂ (A, C) and S@Au@SiO₂ (B, D) nanoparticle cathodes.

S@Au@SiO₂ nanoparticles is ~77%, which is comparable to that of the S@SiO₂ nanoparticles.

Electrochemical Performance of Li–S Batteries. The electrochemical performance of the S@SiO₂ and S@Au@SiO₂ nanoparticles was investigated using a 2032 type coin battery with an electrolyte of 1 M LiTFSI in DOL:DME. Figure 6A shows the cycling performance of the S@SiO₂ nanoparticles for 100 cycles at 0.2 C. The overcharge in the S@SiO₂-based cathode (Figure 6A) is related to minor dissolution and shuttling of polysulfides. This phenomenon is eliminated when Au NPs are decorated into the SiO₂ shell (Figure 6B) due to the interaction and bonding of Au with polysulfides.^{29,30} Importantly, the discharge capacity of the S@SiO₂ electrode in the first cycle reached 1153 mA h g⁻¹ (Figure 6C). Apparent from the data, the battery is able to deliver a repeatable specific capacity of 816 mA h g⁻¹ after 100 cycles. In addition, the capacity retention of the S@SiO₂ battery was 70% with 0.3% capacity decay per cycle at 0.2 C. Meanwhile, the Coulombic efficiency remained at ~99% after 15 cycles.

The initial discharge capacity of the S@Au@SiO₂ battery reached a value similar to that of the S@SiO₂ battery, 1126 mA h g⁻¹, as shown in Figure 6D. However, a faster capacity decay was observed for the S@Au@SiO₂-based battery, shown in Figure 6C,D. Our initial goal was to introduce Au nanoparticles into the material system to reduce capacity decay by (1) facilitating electron transport and (2) introducing a method of trapping discharge products (Li₂S_x, 2 ≤ x ≤ 8), especially highly soluble high-order polysulfides (Li₂S_x, 6 ≤ x ≤ 8) through chemical interactions with the gold.^{7,24,26} Unfortunately, introduction of the Au nanoparticles into the battery system expedited capacity decay at 0.2 C. We hypothesize that the strong chemical interaction between the Au NPs and the highly insoluble low-order polysulfides (Li₂S, Li₂S₂) play an important role in the expedited capacity decay. It is plausible that low-order polysulfides, which prefer to form on the surface of the gold nanoparticles,³⁶ effectively diminish the pore size of the porous SiO₂ shell, hence blocking the transport of Li⁺ ions from outside to inside the S@Au@SiO₂

nanoparticles. Consequently, contact between Li⁺ and the sulfur inside of the SiO₂ shell is inhibited, as illustrated in Figure 7. Hence, the reversible capacity of the S@Au@SiO₂

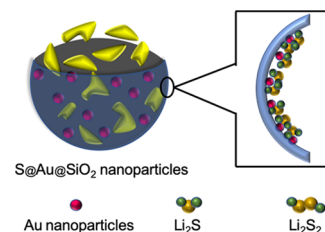


Figure 7. Illustration representing low-order lithium polysulfides attached to the surface of Au NPs; these aggregates can plausibly inhibit the transport of Li⁺ through the porous SiO₂ shell at slow charge/discharge rates.

batteries is ~20% lower than the S@SiO₂ batteries at 0.2 C, regardless of the previously mentioned advantages of introducing gold nanoparticles into the battery system. Nevertheless, compared to other literature examples composed of similar materials (shown in Table 1), our S@SiO₂-based cathode delivered a stable cycling stability with discharge/charge capacity over 800 mA h g⁻¹ after 100 cycles. It is further important to note that Au NPs are oxidatively and reductively stable within the electrochemical window used for the battery tests. Previous studies by Han et al. showed that Au NPs undergo oxidation when the applied voltage is higher than 0.7 V vs SHE;³⁷ importantly, the upper cutoff was 3 V vs Li/Li⁺ in our battery tests, which corresponds to 0 V vs SHE. Furthermore, the reduction of Au by lithium happens below 0.4 V vs Li/Li⁺,³⁸ which is much lower than the lower cut-off voltage of 1.5 V vs Li/Li⁺ used in our studies.

The cycling performance of the S@SiO₂ and S@Au@SiO₂ nanoparticles was evaluated at various rates: 0.2, 0.5, 1, 2, and 5 C. For the S@SiO₂-based cathode, the discharge capacity stabilized at around 900, 800, 720, 630, and 170 mA h g⁻¹, respectively, as shown in Figure 8A. Importantly, the S@Au@

Table 1. Summary of Li–S Battery Performance with SiO₂- or Au-Based Cathodes

material	structure	specific capacity, discharge rate	cycling stability	references
S@SiO ₂	nanospheres	~1400 mA h g ⁻¹ , 0.2 C	441 mA h g ⁻¹ @ 50th	24
S@Au@SiO ₂	nanospheres (core–shell)	1126 mA h g ⁻¹ , 0.2 C	666 mA h g ⁻¹ @ 100th	this work
S/VGCF@SiO ₂ ^a	network-structure	951 mA h g ⁻¹ , 0.5 C	710 mA h g ⁻¹ @ 100th	27
sulfur–silica nanocomposite	raspberry-like morphology	~1200 mA h g ⁻¹ , 0.02 C	~750 mA h g ⁻¹ @ 350th	39
S@SiO ₂ w/mrGO ^b	nanospheres	~1400 mA h g ⁻¹ , 0.2 C	763 mA h g ⁻¹ @ 50th	24
CB-S-Au ^c	3D structure	1107 mA h g ⁻¹ , 0.1 C	771 mA h g ⁻¹ @ 100th	29
S@SiO ₂	nanospheres (core–shell)	1153 mA h g ⁻¹ , 0.2 C	816 mA h g ⁻¹ @ 100th	this work

^aSilica-coated sulfur/vapor-grown carbon fiber composite. ^bSiO₂-coated sulfur particles with mildly reduced graphene oxide. ^cAcetylene black-S with Au nanoparticles.

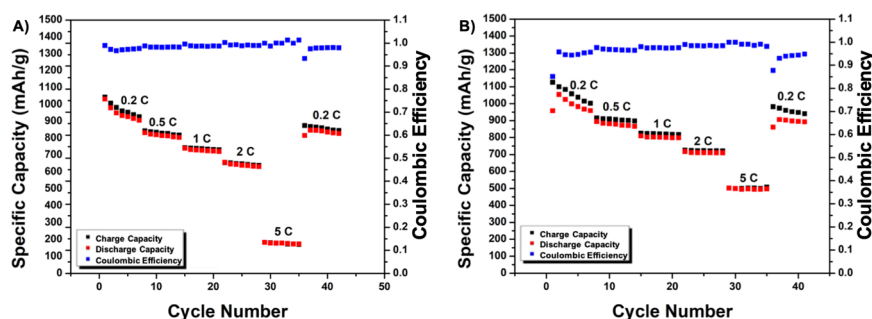


Figure 8. Charge/discharge cycling performance at different current density rates (0.2, 0.5, 1, 2, and 5 C) for the (A) S@SiO₂-based battery and (B) S@Au@SiO₂-based battery.

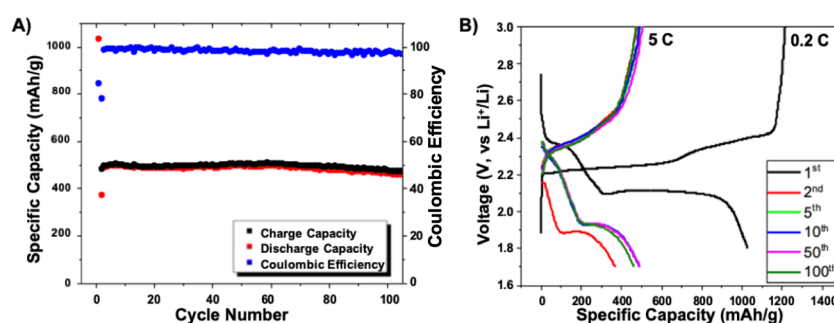


Figure 9. (A) Galvanostatic charge/discharge cycling performance and voltage profiles for the S@Au@SiO₂ (B) nanoparticle cathodes. The first cycle is at a current density 0.2 C and later cycles at 5 C (1 C = 1672 mA g⁻¹).

SiO₂-based cathode showed better performance than the S@SiO₂-based cathode when the rate was increased (see Figure 8B). Notably, at a rate of 5 C, the S@Au@SiO₂ cathode delivered a much higher discharge capacity of 500 mA h g⁻¹ than the 170 mA h g⁻¹ from the S@SiO₂ cathode, suggesting that the Au NPs are able to facilitate electron transport. Therefore, at slow charge/discharge rates, Li⁺ transport appears to be the limiting factor for battery operation (due to the formation of sterically bulky Li₂S_x polysulfide–Au NP aggregates that block Li⁺ transport through the SiO₂ shell). In contrast, at rapid charge/discharge rates (for which the formation of sterically bulky Li₂S_x polysulfide–Au NP aggregates is plausibly limited kinetically), electron transport appears to be the promoting factor.

Figure 9A shows the long cycle performance of the S@Au@SiO₂ cathode evaluated at 5 C. After an initial discharge capacity of ~1050 mA h g⁻¹ under 0.2 C (Figure 9B), the cell delivered a reversible capacity of ~500 mA h g⁻¹ under 5 C with a 96% capacity retention after 100 cycles. Moreover, when the S@Au@SiO₂ cathode was tested under a high rate of 5 C, the capacity retention after 100 cycles was much improved compared to that at 0.2 C. It is likely that the shortened

discharge/charge times at 5 C alleviated detrimental dissolution of soluble polysulfide species and thereby enhanced capacity retention.

CONCLUSIONS

In this study, core–shell S@SiO₂ and S@Au@SiO₂ nanoparticles possessing porous thin SiO₂ shells were successfully synthesized as cathode materials for lithium–sulfur batteries using Fe(NO₃)₃ as a key reagent in the conversion of ZnS nanoparticle cores to elemental sulfur cores with markedly diminished volume. The cycle efficiency of both nanoparticles as cathode materials in lithium–sulfur batteries was also evaluated. The S@SiO₂-based cathode had an initial discharge capacity of 1153 mA h g⁻¹ and stabilized at 816 mA h g⁻¹ after 100 cycles at 0.2 C. By comparison, the discharge capacity of the S@Au@SiO₂-based cathode reached a similar value in the first cycle, but stabilized at a lower value compared to the S@SiO₂-based cathode, 666 mA h g⁻¹, after 100 cycles at 0.2 C. At these slow current density rates, we propose that the S@Au@SiO₂ system suffers from the formation of sterically bulky Li₂S_x polysulfide–Au NP aggregates on the inner surface of the SiO₂

shell, which inhibits Li^+ transport through the shell and impedes the cycling performance of our battery system. However, owing to enhanced electron transport, the S@Au@SiO_2 -based cathode can provide a higher reversible capacity of 500 mA h g^{-1} at 5 C with a capacity retention of 96% after 100 cycles. Given these results as a whole, the present investigation illustrates the beneficial effects of incorporating Au nanoparticles into S@SiO_2 -based cathodes over a range of charging/discharging rates. Given the encouraging results, our future work will explore various modifications of the nanomaterials to enhance battery capacity under the lean electrolyte condition.

ASSOCIATED CONTENT

Supporting Information

The Supporting Information is available free of charge at <https://pubs.acs.org/doi/10.1021/acsami.0c10341>.

Figure S1 shows voltage profiles at a current density of 0.2 C for S@SiO_2 and S@Au@SiO_2 nanoparticle cathodes with a lean electrolyte of $5 \mu\text{L mg}^{-1}$ (PDF)

AUTHOR INFORMATION

Corresponding Authors

Yan Yao – Department of Electrical and Computer Engineering and Texas Center for Superconductivity, University of Houston, Houston, Texas 77204, United States; Email: yyao4@uh.edu

T. Randall Lee – Department of Chemistry and Texas Center for Superconductivity, University of Houston, Houston, Texas 77204, United States; orcid.org/0000-0001-9584-8861; Email: trlee@uh.edu

Authors

Tingting Liu – Department of Chemistry and Texas Center for Superconductivity, University of Houston, Houston, Texas 77204, United States

Ye Zhang – Department of Electrical and Computer Engineering and Texas Center for Superconductivity, University of Houston, Houston, Texas 77204, United States

Chien-Hung Li – Department of Medicinal and Applied Chemistry, Kaohsiung Medical University, Kaohsiung 807, Taiwan; orcid.org/0000-0003-1643-8368

Maria D. Marquez – Department of Chemistry and Texas Center for Superconductivity, University of Houston, Houston, Texas 77204, United States

Hung-Vu Tran – Department of Chemistry and Texas Center for Superconductivity, University of Houston, Houston, Texas 77204, United States; orcid.org/0000-0001-8536-2737

Francisco C. Robles Hernández – Department of Electrical and Computer Engineering and Department of Engineering Technology, and Materials Science and Engineering, University of Houston, Houston, Texas 77204, United States

Complete contact information is available at:

<https://pubs.acs.org/doi/10.1021/acsami.0c10341>

Notes

The authors declare no competing financial interest.

ACKNOWLEDGMENTS

The authors are grateful to Dr Jianhua Gu from the Houston Methodist Research Institute for training and assistance in measuring SEM-EDX on the Nova NanoSEM 230 microscope and Dr Tatyana Makarenko at the University of Houston for

acquiring the TGA data. The authors also acknowledge the Air Force Office of Scientific Research (AFOSR FA9550-18-1-0094, T.R.L.), the Robert A. Welch Foundation (Grant no. E-1320, T.R.L.), Scialog from Research Corporation for Science Advancement (Grant no. 27110, Y.Y.), and the Texas Center for Superconductivity (T.R.L. and Y.Y.) for providing financial support for this research.

REFERENCES

- (1) Seh, Z. W.; Li, W.; Cha, J. J.; Zheng, G.; Yang, Y.; McDowell, M. T.; Hsu, P.-C.; Cui, Y. Sulfur-TiO₂ Yolk-Shell Nanoarchitecture with Internal Void Space for Long-Cycle Lithium Sulfur Batteries. *Nat. Commun.* **2013**, *4*, No. 1331.
- (2) Ma, Y.; Zhang, H.; Wu, B.; Wang, M.; Li, X.; Zhang, H. Lithium Sulfur Primary Battery with Super High Energy Density: Based on the Cauliflower-like Structured C/S Cathode. *Sci. Rep.* **2015**, *5*, No. 14949.
- (3) Yang, Y.; Zheng, G.; Cui, Y. Nanostructured Sulfur Cathodes. *Chem. Soc. Rev.* **2013**, *42*, 3018–3032.
- (4) Wang, J.; Yin, L.; Jia, H.; Yu, H.; He, Y.; Yang, J.; Monroe, C. W. Hierarchical Sulfur-Based Cathode Materials with Long Cycle Life for Rechargeable Lithium Batteries. *ChemSusChem* **2014**, *7*, 563–569.
- (5) Li, W.; Zhang, W.; Zheng, G.; Seh, Z. W.; Yao, H.; Cui, Y. Understanding the Role of Different Conductive Polymers in Improving the Nanostructured Sulfur Cathode Performance. *Nano Lett.* **2013**, *13*, 5534–5540.
- (6) Xue, M.; Zhou, Y.; Geng, J.; Zeng, P.; Xu, Y.; Wang, Y.; Tang, W.; Wu, P.; Wei, S.; Zhou, Y. Hollow Porous SiO₂ Nanobelts Containing Sulfur for Long-Life Lithium-Sulfur Batteries. *RSC Adv.* **2016**, *6*, 91179–91184.
- (7) Manthiram, A.; Fu, Y.; Chung, S.-H.; Zu, C.; Su, Y.-S. Rechargeable Lithium–Sulfur Batteries. *Chem. Rev.* **2014**, *114*, 11751–11787.
- (8) Yuan, H.; Peng, H.-J.; Huang, J.-Q.; Zhang, Q. Sulfur Redox Reactions at Working Interfaces in Lithium–Sulfur Batteries: A Perspective. *Adv. Mater. Interfaces* **2019**, *6*, No. 1802046.
- (9) Choudhury, S.; Zeiger, M.; Massuti-Ballester, P.; Fleischmann, S.; Formanek, P.; Borhardt, L.; Presser, V. Carbon Onion-Sulfur Hybrid Cathodes for Lithium-Sulfur Batteries. *Sustainable Energy Fuels* **2017**, *1*, 84–94.
- (10) Jayaprakash, N.; Shen, J.; Moganty, S. S.; Corona, A.; Archer, L. A. Porous Hollow Carbon@Sulfur Composites for High-Power Lithium-Sulfur Batteries. *Angew. Chem., Int. Ed.* **2011**, *50*, 5904–5908.
- (11) Wang, H.; Yang, Y.; Liang, Y.; Robinson, J. T.; Li, Y.; Jackson, A.; Cui, Y.; Dai, H. Graphene-Wrapped Sulfur Particles as a Rechargeable Lithium-Sulfur Battery Cathode Material with High Capacity and Cycling Stability. *Nano Lett.* **2011**, *11*, 2644–2647.
- (12) Yu, M.; Li, R.; Wu, M.; Shi, G. Graphene Materials for Lithium-Sulfur Batteries. *Energy Storage Mater.* **2015**, *1*, 51–73.
- (13) Zhou, W.; Yu, Y.; Chen, H.; DiSalvo, F. J.; Abruña, H. D. Yolk-Shell Structure of Polyaniline Coated Sulfur for Lithium Sulfur Batteries. *J. Am. Chem. Soc.* **2013**, *135*, 16736–16743.
- (14) Yang, Y.; Yu, G.; Cha, J. J.; Wu, H.; Vosgueritchian, M.; Yao, Y.; Bao, Z.; Cui, Y. Improving the Performance of Lithium-Sulfur Batteries by Conductive Polymer Coating. *ACS Nano* **2011**, *5*, 9187–9193.
- (15) Xie, J.; Li, B.-Q.; Peng, H.-J.; Song, Y.-W.; Zhao, M.; Chen, X.; Zhang, Q.; Huang, J.-Q. Implanting Atomic Cobalt within Mesoporous Carbon toward Highly Stable Lithium–Sulfur Batteries. *Adv. Mater.* **2019**, *31*, No. 1903813.
- (16) He, J.; Manthiram, A. Long-Life, High-Rate Lithium–Sulfur Cells with a Carbon-Free VN Host as an Efficient Polysulfide Adsorbent and Lithium Dendrite Inhibitor. *Adv. Energy Mater.* **2020**, *10*, No. 1903241.
- (17) Hwang, J.-Y.; Kim, H. M.; Lee, S.-K.; Lee, J.-H.; Abouimrane, A.; Khaleel, M. A.; Belharouak, I.; Manthiram, A.; Sun, Y.-K. High-Energy, High-Rate, Lithium-Sulfur Batteries: Synergetic Effect of

Hollow TiO₂-Webbed Carbon Nanotubes and a Dual Functional Carbon-Paper Interlayer. *Adv. Energy Mater.* **2016**, *6*, No. 1501480.

(18) Ma, X. Z.; Jin, B.; Wang, H. Y.; Hou, J. Z.; Zhong, X. B.; Wang, H. H.; Xin, P. M. S-TiO₂ Composite Cathode Materials for Lithium/Sulfur Batteries. *J. Electroanal. Chem.* **2015**, *736*, 127–131.

(19) Liu, X.; Shan, Z.; Zhu, K.; Du, J.; Tang, Q.; Tian, J. Sulfur Electrode Modified by Bifunctional Nafion/ γ -Al₂O₃ Membrane for High Performance Lithium-Sulfur Batteries. *J. Power Sources* **2015**, *274*, 85–93.

(20) Yu, Q.; Luo, R.; Bai, X.; Yang, W.; Lu, Y.; Hou, X.; Peng, T.; Liu, X.; Kim, J. K.; Luo, Y. Rational Design of Double-Confined Mn₂O₃/S@Al₂O₃ Nanocube Cathodes for Lithium-Sulfur Batteries. *J. Solid State Electrochem.* **2018**, *22*, 849–858.

(21) Rehman, S.; Guo, S.; Hou, Y. Rational Design of Si/SiO₂@Hierarchical Porous Carbon Spheres as Efficient Polysulfide Reservoirs for High-Performance Li-S Battery. *Adv. Mater.* **2016**, *28*, 3167–3172.

(22) Choi, S.; Su, D.; Shin, M.; Park, S.; Wang, G. Pomegranate-Structured Silica/Sulfur Composite Cathodes for High-Performance Lithium-Sulfur Batteries. *Chem. - Asian J.* **2018**, *13*, 568–576.

(23) Zhao, Q.; Zheng, J.; Archer, L. Interphases in Lithium-Sulfur Batteries: Toward Deployable Devices with Competitive Energy Density and Stability. *ACS Energy Lett.* **2018**, *3*, 2104–2113.

(24) Campbell, B.; Bell, J.; Hosseini Bay, H.; Favors, Z.; Ionescu, R.; Ozkan, C. S.; Ozkan, M. SiO₂-Coated Sulfur Particles with Mildly Reduced Graphene Oxide as a Cathode Material for Lithium-Sulfur Batteries. *Nanoscale* **2015**, *7*, 7051–7055.

(25) Pan, H.; Huang, X.; Zhang, R.; Zhang, T.; Chen, Y.; Hoang, T. K. A.; Wen, G. Reduced Graphene Oxide-Encapsulated Mesoporous Silica as Sulfur Host for Lithium-Sulfur Battery. *J. Solid State Electrochem.* **2018**, *22*, 3557–3568.

(26) Wu, H.; Tang, Q.; Fan, H.; Liu, Z.; Hu, A.; Zhang, S.; Deng, W.; Chen, X. Dual-Confined and Hierarchical-Porous Graphene/C/SiO₂ Hollow Microspheres through Spray Drying Approach for Lithium-Sulfur Batteries. *Electrochim. Acta* **2017**, *255*, 179–186.

(27) Li, J.; Guo, J.; Zeng, L.; Huang, Y.; Peng, R. Improving Lithium-Sulfur Battery Performance by Using Ternary Hybrid Cathode Material. *RSC Adv.* **2016**, *6*, 26630–26636.

(28) Li, J.; Huang, Y.; Zhang, S.; Jia, W.; Wang, X.; Guo, Y.; Jia, D.; Wang, L. Decoration of Silica Nanoparticles on Polypropylene Separator for Lithium-Sulfur Batteries. *ACS Appl. Mater. Interfaces* **2017**, *9*, 7499–7504.

(29) Fan, C.-Y.; Xiao, P.; Li, H.-H.; Wang, H. F.; Zhang, L.-L.; Sun, H.-Z.; Wu, X.-L.; Xie, H.-M.; Zhang, J.-P. Nanoscale Polysulfides Reactors Achieved by Chemical Au-S Interaction: Improving the Performance of Li-S Batteries on the Electrode Level. *ACS Appl. Mater. Interfaces* **2015**, *7*, 27959–27967.

(30) Depardieu, M.; Demir-Cakan, R.; Sanchez, C.; Birot, M.; Deleuze, H.; Morcrette, M.; Backov, R. On the Effect of Gold Nanoparticles Loading within Carbonaceous Macro-Mesocellular Foams toward Lithium-Sulfur Battery Performances. *Solid State Sci.* **2016**, *55*, 112–120.

(31) Xu, X.; Hu, L.; Gao, N.; Liu, S.; Wageh, S.; Al-Ghamdi, A. A.; Alshahrie, A.; Fang, X. Controlled Growth from ZnS Nanoparticles to ZnS-CdS Nanoparticle Hybrids with Enhanced Photoactivity. *Adv. Funct. Mater.* **2015**, *25*, 445–454.

(32) Kim, J.; Bryan, W. W.; Lee, T. R. Preparation, Characterization, and Optical Properties of Gold, Silver, and Gold - Silver Alloy Nanoshells Having Silica Cores. *Langmuir* **2008**, *24*, 11147–11152.

(33) Stöber, W.; Fink, A.; Bohn, E. Controlled Growth of Monodispersed Silica Spheres in the Micron Size Range. *J. Colloid Interface Sci.* **1968**, *26*, 62–69.

(34) Du, H.; Gui, X.; Yang, R.; Lin, Z.; Liang, B.; Chen, W.; Zheng, Y.; Zhu, H.; Chen, J. In-Situ Sulfur Loading in Graphene-Like Nano-Cell by Template-Free Method for Li-S Batteries. *Nanoscale* **2018**, *10*, 3877–3883.

(35) Zuber, K.; Evans, D. R.; McClure, S.; Murphy, P. J. Mesoporous Siloxane Films Through Thermal Oxidation of

Siloxane-Carbon Nanocomposites. *Adv. Eng. Mater.* **2015**, *17*, 1547–1555.

(36) Babu, G.; Ababtain, K.; Ng, K. Y. S.; Arava, L. M. R. Electrocatalysis of Lithium Polysulfides: Current Collectors as Electrodes in Li/S Battery Configuration. *Sci. Rep.* **2015**, *5*, No. 8763.

(37) Han, D.; Kim, S.; Kim, Y.; Sohn, B.; Chung, T. D. Surface Coverage and Size Effects on Electrochemical Oxidation of Uniform Gold Nanoparticles. *Electrochem. Commun.* **2015**, *53*, 11–14.

(38) Yan, K.; Lu, Z.; Lee, H.; Xiong, F.; Hsu, P.; Li, P.; Zhao, J.; Chu, S.; Cui, Y. Selective Deposition and Stable Encapsulation of Lithium through Heterogeneous Seeded Growth. *Nat. Energy* **2016**, *1*, 16010.

(39) Lodi-Marzano, F.; Leuthner, S.; Sommer, H.; Brezesinski, T.; Janek, J. High-Performance Lithium-Sulfur Batteries using Yolk-Shell Type Sulfur-Silica Nanocomposite Particles with Raspberry-Like Morphology. *Energy Technol.* **2015**, *3*, 830–833.